J|A|C|S ARTICLES

Published on Web 02/13/2009

Self-Assembled Simple Hexagonal AB_2 Binary Nanocrystal Superlattices: SEM, GISAXS, and Defects

Danielle K. Smith,[†] Brian Goodfellow,[†] Detlef-M. Smilgies,[‡] and Brian A. Korgel*,[†]

Department of Chemical Engineering, Texas Materials Institute, Center for Nano- and Molecular Science and Technology, The University of Texas at Austin, Austin, Texas 78712-1062 and Cornell High Energy Synchrotron Source (CHESS), Cornell University, Ithaca, New York 14853

Received November 6, 2008; E-mail: korgel@che.utexas.edu

Abstract: Binary superlattices (BSLs) of sterically stabilized, hydrophobic, large (A; 11.5 nm diameter) Fe_2O_3 and small (B; 6.1 nm diameter) Au nanocrystals were assembled by slow evaporation of colloidal dispersions on tilted substrates. A detailed analysis of the BSL structure was carried out using transmission and scanning electron microscopy (TEM and SEM) and grazing incidence small-angle X-ray scattering (GISAXS). The BSLs were simple hexagonal (sh) AB_2 superlattices (isostructural with the compound AlB_2; space group 191, *P6/mmm*) of large nanocrystals occupying a simple hexagonal lattice with small nanocrystals in the interstitial spaces. SEM and GISAXS confirmed long-range order of the BSLs and GISAXS revealed that the superlattice is slightly contracted (8−12%) perpendicular to the substrate as a result of solvent drying in the deposition process. When the sh-AB_2 superlattice deposits on a (100) plane, this shrinkage occurs in the [210] direction and changes the lattice symmetry to centered orthorhombic. Additionally, nearly periodic superlattice dislocations consisting of inserted half-planes of gold nanocrystals were observed by SEM in some BSLs.

Introduction

Binary nanocrystal superlattices (BSLs)—e.g., periodically ordered arrays of nanocrystals with two different well-defined diameters—have been reported with astonishingly diverse structures, including those that are isostructural with AlB_2,[1−8] CaB_6,[2,3] $CaCu_5$,[1−3,5,7,9,10] CuAu,[2,3,5,10] Cu_3Au,[2,3] $NaZn_{13}$,[1−4,7,11] Fe_4C,[2,3] $MgNi_2$,[2] $MgZn_2$,[2,3,7] NaCl,[2−4,12,13] and NiAs[4] compounds. Since nanocrystals can be synthesized with a wide variety of chemical and physical properties, including magnets,[14] metals,[15] semiconductors,[16] and even more complex multifunctional heterostructures,[16−25] they provide a library of assorted materials suited for new technologies in the biological sciences,[26−29] computing and information storage,[14,30] photovoltaics,[31] and thermoelectrics.[13] By merging nanocrystals into

[†] University of Texas at Austin.
[‡] Cornell University.

(1) Redl, F. X.; Cho, K. S.; Murray, C. B.; O'Brien, S. *Nature* **2003**, *423*, 968–971.
(2) Shevchenko, E. V.; Talapin, D. V.; Kotov, N. A.; O'Brien, S.; Murray, C. B. *Nature* **2006**, *439*, 55–59.
(3) Shevchenko, E. V.; Talapin, D. V.; Murray, C. B.; O'Brien, S. *J. Am. Chem. Soc.* **2006**, *128*, 3620–3637.
(4) Shevchenko, E. V.; Kortright, J. B.; Talapin, D. V.; Aloni, S.; Alivisatos, A. P. *Adv. Mater.* **2007**, *19*, 4183–4188.
(5) Shevchenko, E. V.; Ringler, M.; Schwemer, A.; Talapin, D. V.; Klar, T. A.; Rogach, A. L.; Feldmann, J.; Alivisatos, A. P. *J. Am. Chem. Soc.* **2008**, *130*, 3274–3275.
(6) Overgaag, K.; Evers, W.; de Nijs, B.; Koole, R.; Meeldijk, J.; Vanmaekelbergh, D. *J. Am. Chem. Soc.* **2008**, *130*, 7833–7835.
(7) Chen, Z.; O'Brien, S. *ACS Nano* **2008**, *2*, 1219–1229.
(8) Kiely, C. J.; Fink, J.; Brust, M.; Bethell, D.; Schiffrin, D. J. *Nature* **1998**, *396*, 444–446.
(9) Chen, Z. Y.; Moore, J.; Radtke, G.; Sirringhaus, H.; O'Brien, S. *J. Am. Chem. Soc.* **2007**, *129*, 15702–15709.
(10) Lu, C.; Chen, Z.; O'Brien, S. *Chem. Mater.* **2008**, *20*, 3594–3600.
(11) Shevchenko, E. V.; Talapin, D. V.; O'Brien, S.; Murray, C. B. *J. Am. Chem. Soc.* **2005**, *127*, 8741–8747.
(12) Saunders, A. E.; Korgel, B. A. *ChemPhysChem* **2005**, *6*, 61–65.
(13) Urban, J. J.; Talapin, D. V.; Shevchenko, E. V.; Kagan, C. R.; Murray, C. B. *Nat. Mater.* **2007**, *6*, 115–121.
(14) Lee, D. C.; Smith, D. K.; Heitsch, A. T.; Korgel, B. A. *Annu. Rep. Prog. Chem., Sect. C: Phys. Chem.* **2007**, *103*, 351–402.
(15) Liz-Marzan, L. M. *Mater. Today* **2004**, *7*, 26–31.
(16) Jun, Y. W.; Choi, J. S.; Cheon, J. *Angew. Chem., Int. Ed.* **2006**, *45*, 3414–3439.
(17) Buonsanti, R.; Grillo, V.; Carlino, E.; Giannini, C.; Curri, M. L.; Innocenti, C.; Sangregorio, C.; Achterhold, K.; Parak, F. G.; Agostiano, A.; Cozzoli, P. D. *J. Am. Chem. Soc.* **2006**, *128*, 16953–16970.
(18) Carbone, L.; Kudera, S.; Giannini, C.; Ciccarella, G.; Cingolani, R.; Cozzoli, P. D.; Manna, L. *J. Mater. Chem.* **2006**, *16*, 3952–3956.
(19) Choi, J. S.; Jun, Y. W.; Yeon, S. I.; Kim, H. C.; Shin, J. S.; Cheon, J. *J. Am. Chem. Soc.* **2006**, *128*, 15982–15983.
(20) Cozzoli, P. D.; Pellegrino, T.; Manna, L. *Chem. Soc. Rev.* **2006**, *35*, 1195–1208.
(21) Kudera, S.; Carbone, L.; Casula, M. F.; Cingolani, R.; Falqui, A.; Snoeck, E.; Parak, W. J.; Manna, L. *Nano Lett.* **2005**, *5*, 445–449.
(22) Kwon, K. W.; Lee, B. H.; Shim, M. *Chem. Mater.* **2006**, *18*, 6357–6363.
(23) Pellegrino, T.; Fiore, A.; Carlino, E.; Giannini, C.; Cozzoli, P. D.; Ciccarella, G.; Respaud, M.; Palmirotta, L.; Cingolani, R.; Manna, L. *J. Am. Chem. Soc.* **2006**, *128*, 6690–6698.
(24) Shi, W. L.; Zeng, H.; Sahoo, Y.; Ohulchanskyy, T. Y.; Ding, Y.; Wang, Z. L.; Swihart, M.; Prasad, P. N. *Nano Lett.* **2006**, *6*, 875–881.
(25) Yu, H.; Chen, M.; Rice, P. M.; Wang, S. X.; White, R. L.; Sun, S. H. *Nano Lett.* **2005**, *5*, 379–382.
(26) Alivisatos, A. P. *Nat. Biotechnol.* **2004**, *22*, 47–52.
(27) Durr, N. J.; Larson, T.; Smith, D. K.; Korgel, B. A.; Sokolov, K.; Ben-Yakar, A. *Nano Lett.* **2007**, *7*, 941–945.
(28) Lee, J. H.; Huh, Y. M.; Jun, Y.; Seo, J.; Jang, J.; Song, H. T.; Kim, S.; Cho, E. J.; Yoon, H. G.; Suh, J. S.; Cheon, J. *Nat. Med.* **2007**, *13*, 95–99.
(29) Michalet, X.; Pinaud, F. F.; Bentolila, L. A.; Tsay, J. M.; Doose, S.; Li, J. J.; Sundaresan, G.; Wu, A. M.; Gambhir, S. S.; Weiss, S. *Science* **2005**, *307*, 538–544.
(30) Zeng, H.; Li, J.; Liu, J. P.; Wang, Z. L.; Sun, S. *Nature* **2002**, *420*, 395–398.

BSLs, *metamaterials* may be fabricated with new, unique characteristics that result from their nanoscale organization and interplay of their constituent properties.[32] For example, magnetic and semiconductor nanocrystals might be mixed to form new breeds of magneto-optic materials,[11] mixtures of different magnetic nanocrystals may lead to higher energy density magnetic properties,[30,33] and mixtures of semiconductors may be used for optoelectronic applications, like higher performance photovoltaics.[34] In one study that exemplifies this idea, BSLs of PbTe and Ag_2Te nanocrystals were over 100× more electrically conductive than superlattices of only PbTe or Ag_2Te nanocrystals.[13]

To design and engineer BSL properties, their assembly must be well understood. Some BSL structures are expected based on geometrical packing arguments for spheres, as in the case of cubic AB (NaCl) and simple hexagonal AB_2 (AlB_2) structures in which nanocrystals fill space as efficiently as possible.[34] But many observed BSL structures, such as cub-AB_{13},[11] $CaCu_5$,[1−3,5,7,9,10] Fe_4C,[2,3] Cu_3Au,[2,3] are not *closest*-packed arrangements.[35] Therefore, a variety of other factors in addition to space-filling arguments have been proposed to be important in determining BSL structure, including size- and composition-dependent interparticle forces, including van der Waals attractions,[36,37] ligand−ligand interactions,[38] capillary forces,[39] electrostatic interactions,[2] and kinetic factors.[3,9,40] But the matter is complicated by the fact that the BSL structures reported thus far have had relatively small grain size (<3 μm) and structural characterization has been carried out almost exclusively by transmission electron microscopy (TEM) of relatively thin samples. To date, no scanning electron microscopy (SEM) images or small-angle X-ray scattering patterns (SAXS) of BSLs have been published, and it is therefore possible that some observed BSLs are only metastable or stabilized/induced by the substrate; thus, making it more complicated to identify the underlying forces responsible for BSL structure.

Herein, SEM and grazing incidence small-angle X-ray scattering (GISAXS) measurements of sh-AB_2 BSLs are presented, which confirm the existence of long-range order in sh-AB_2 BSLs. This data provides evidence that the sh-AB_2 BSL phase is indeed a thermodynamically stable phase for the nanocrystal size ratio studied here (0.53). BSLs, however, only formed when nanocrystals were deposited onto a tilted substrate by controlled slow evaporation from dispersions with excess oleic acid. This indicates that the forces driving BSL formation are relatively weak. Some diversity in BSL structure was nonetheless also observed, including (1) uniaxial superlattice shrinkage normal to the substrate from residual solvent evaporation; (2) nearly periodic dislocations consisting of inserted half-planes of Au nanocrystals; and in thin BSL layers, (3) an analog of an AB_{13} phase in which Fe_2O_3 nanocrystals have substituted for Au nanocrystals in the 8a Wyckoff positions in the unit cell of space group 226, and (4) an "expanded" sh-AB_2 (100) plane.

Experimental section

Materials and Supplies. All chemicals were used as received. Iron pentacarbonyl ($Fe(CO)_5$, 99.999%), oleic acid (99%), hydrogen tetrachloroaurate(III) hydrate (99.9+%), tetraoctylammonium bromide (TOAB, 98%), sodium borohydride ($NaBH_4$, 98+%), and dodecanethiol (≥98%) were purchased from Sigma-Aldrich. Dioctyl ether (>97%) was purchased from Fluka. Toluene (99.9%) was purchased from Fisher. Doubly distilled deionized water (DI-H_2O) was used in all preparations.

Au Nanocrystal Synthesis. Dodecanethiol-coated 6.1 nm diameter Au nanocrystals were prepared as previously described.[41,42] In a 50 mL Erlenmeyer flask, 0.19 g of hydrogen tetrachloroaurate(III) hydrate was dissolved in 18 mL of DI water. 1.35 g of TOAB dissolved in 12.25 mL of toluene was added to the aqueous solution, and the mixture was stirred for 1 h. The aqueous phase was discarded. A solution of 0.25 g of $NaBH_4$ dissolved in 15 mL of DI water was then added to the organic solution. This mixture was stirred for 20 h. The aqueous phase was then discarded. A volume of 120 μL of dodecanethiol was added to the organic phase and the mixture was stirred for 1 h.

The Au nanocrystals were isolated by first centrifuging the solution for 3 min at 8000 rpm and discarding the precipitate, which consists of poorly capped nanocrystals. The supernatant was collected and excess ethanol was added to precipitate the nanocrystals and separate them from molecular impurities in the reaction. After centrifuging the solution for 8 min at 8500 rpm, the precipitate was collected and the supernatant discarded. The nanocrystals were redispersed in chloroform, followed by size-selective precipitation using ethanol as an antisolvent.[36,43] 6.1 ± 0.73 (±12%) nm diameter Au nanocrystals were used for superlattice self-assembly.

Fe_2O_3 Nanocrystal Synthesis. Oleic acid-coated 11.5 nm diameter Fe_2O_3 nanocrystals with a 6% polydispersity were prepared under inert (N_2) atmosphere using standard glovebox and Schlenk line techniques and published procedures.[44] In a 25 mL three neck flask, 10 mL of dioctyl ether and 960 μL (4.56 mmol) of oleic acid were heated to 100 °C under N_2 flow at atmospheric pressure. 0.2 mL (1.52 mmol) of $Fe(CO)_5$ was injected into this solution. [Caution must be taken when preparing $Fe(CO)_5$, as it is extremely volatile and potentially hazardous (refer to MSDS before use).] The solution was refluxed at 300 °C for 1 h. The reaction flask was removed from the heating mantle and allowed to cool to room

(31) Gur, I.; Fromer, N. A.; Geier, M. L.; Alivisatos, A. P. *Science* **2005**, *310*, 462–465.
(32) Rogach, A. L. *Angew. Chem., Int. Ed.* **2004**, *43*, 148–149.
(33) Cheon, J.; Park, J. I.; Choi, J. S.; Jun, Y. W.; Kim, S.; Kim, M. G.; Kim, Y. M.; Kim, Y. J. *Proc. Natl. Acad. Sci.* **2006**, *103*, 3023–3027.
(34) Collier, C. P.; Vossmeyer, T.; Heath, J. R. *Annu. Rev. Phys. Chem.* **1998**, *49*, 371–404.
(35) For example, the maximum packing fractions for superlattices with fcc-AB (rock salt) and sh-AB_2 (AlB_2) structures are 0.793 and 0.778, respectively; whereas, the maximum packing fractions of the ico-AB_{13}, cub-AB_{13}, and $CaCu_5$ structures are 0.738, 0.7, and 0.7, respectively. A face-centered cubic lattice of monodisperse nanocrystals has a packing fraction of 0.74, which is more dense than the ico-AB_{13}, cub-AB_{13} and $CaCu_5$ lattices that would be formed by a bidisperse mixture of nanocrystals. The packing fractions also depend on the actual particle size ratio and are maximized when the smaller nanocrystals fit perfectly into the interstitial spaces within a lattice composed of the larger nanocrystals—i.e., 0.414 for cub-AB and 0.53 for sh-AB_2.
(36) Korgel, B. A.; Fullam, S.; Connolly, S.; Fitzmaurice, D. *J. Phys. Chem. B* **1998**, *102*, 8379–8388.
(37) Korgel, B. A.; Fitzmaurice, D. *Phys. Rev. B* **1999**, *59*, 14191–14201.
(38) Luedtke, W. D.; Landman, U. *J. Phys. Chem.* **1996**, *100*, 13323–13329.
(39) Rabideau, B. D.; Bonnecaze, R. T. *Langmuir* **2004**, *20*, 9408–9414.
(40) The issue of how subtle forces and packing density influence superlattice structure is a rich topic. For example, the packing density, coordination number and local packing geometry are equivalent for face-centered cubic (fcc) and hexagonal close-packed (hcp) structures, yet fcc superlattices tend to be favored because there is a small entropy increase when the close packed planes of the superlattice stack into a cubic structure with *ABC* stacking instead of the *ABAB* stacking of an hcp lattice. Relatively slight differences in interparticle interactions have been shown to lead to changes in superlattice structure; for example, by increasing the ratio of the ligand length to the radius of the inorganic core, the superlattice changes from fcc to body-centered cubic (bcc).[37,61]
(41) Sigman, M. B.; Saunders, A. E.; Korgel, B. A. *Langmuir* **2004**, *20*, 978–983.
(42) Brust, M.; Walker, M.; Bethell, D.; Schiffrin, D. J.; Whyman, R. *Chem. Commun.* **1994**, 801–802.
(43) Murray, C. B.; Norris, D. J.; Bawendi, M. G. *J. Am. Chem. Soc.* **1993**, *115*, 8706–8715.
(44) Hyeon, T.; Lee, S. S.; Park, J.; Chung, Y.; Bin Na, H. *J. Am. Chem. Soc.* **2001**, *123*, 12798–12801.

temperature. The flask was then opened to air for 30 min to oxidize the as-made Fe nanocrystals. This reaction solution containing the resulting Fe_2O_3 nanocrystals was then centrifuged for 5 min at 8000 rpm. The supernatant was collected and the precipitate, which consists of solid byproducts and poorly capped nanocrystals, was discarded. Excess ethanol was then added to the supernatant to precipitate the nanocrystals. This mixture was centrifuged for 10 min at 8000 rpm. The supernatant was discarded. The nanocrystals were further purified with two additional reprecipitation and centrifugation steps using hexane and ethanol as a solvent/antisolvent pair. 11.54 ± 0.66 (±6%) nm diameter Fe_2O_3 nanocrystals were used for superlattice self-assembly.

Binary Nanocrystal Superlattice (BSL) Preparation. BSLs were deposited on various substrates, including TEM grids (carbon-coated copper 200 mesh, Electron Microscopy Sciences), Si wafers covered with native oxide (SEH America), or Si_3N_4-coated Si wafers, by immersing the substrate in a glass vial tilted at approximately 65° from vertical with a small volume of nanocrystal dispersion (see Supporting Information for details). The nanocrystal dispersion was made by adding 0.12 mg of Au nanocrystals, 0.1 mg of Fe_2O_3 nanocrystals and 0.1 μL oleic acid in 440 μL of toluene, corresponding to a Fe_2O_3:Au nanocrystal number ratio of 1:2.5. The solvent was then allowed to evaporate over the course of several hours at 45 °C in air.

Materials Characterization. Transmission electron microscopy (TEM) was performed on either a Phillips EM208 TEM with 80 kV accelerating voltage or a JEOL 2010F with the field emission gun operated at 200 kV. Images were acquired digitally. Electron diffraction patterns were simulated using JEMS Electron Microscopy Software Package (Version 3.2710U2008, Copyright: P. Stadelmann, 1999−2008). Scanning electron microscopy (SEM) was performed on a Zeiss Supra 40 SEM with an in-lens arrangement at 10 keV working voltage and 5 mm lens to detector distance. Samples were grounded using copper tape to prevent charging.

Grazing incidence small-angle X-ray scattering (GISAXS) measurements were performed on beam line D1 of the Cornell High Energy Synchrotron Source (CHESS) using monochromatic radiation of wavelength $\lambda = 1.252$ Å with a bandwidth $\Delta\lambda/\lambda$ of 1.5%. The X-ray beam was produced by a hardbent dipole magnet in the Cornell storage ring and monochromatized with Mo:B_4C multilayers with a period of 30 Å. The D1 area detector (MedOptics) is a fiber coupled CCD camera with a pixel size of 46.9 μm by 46.9 μm and a total of 1024 × 1024 pixels with a 14-bit dynamical range per pixel.[45] Typical read-out time per image was below 5 s. The images were dark current corrected, distortion-corrected, and flat-field corrected by the acquisition software. The sample to detector distance was 935 mm, as determined using a silver behenate powder standard. The incident angle of the X-ray beam was varied from 0.05° to 0.25° and typical exposure times were 100 s. Scattering images were calibrated and integrated using the Fit2D software.[46] The GISAXS diffraction peaks were indexed using NANOCELL[47] and our own software.[48]

Results and Discussion

TEM and SEM. Figure 1 shows SEM images of BSLs of (A) 11.5 nm Fe_2O_3 and (B) 6.1 nm Au nanocrystals. The BSLs have a simple hexagonal (sh) AB_2 (AlB_2, space group 191, *P6/mmm*) structure as described in previous reports.[1−7] In the BSL, the large Fe_2O_3 nanocrystals occupy a simple hexagonal lattice

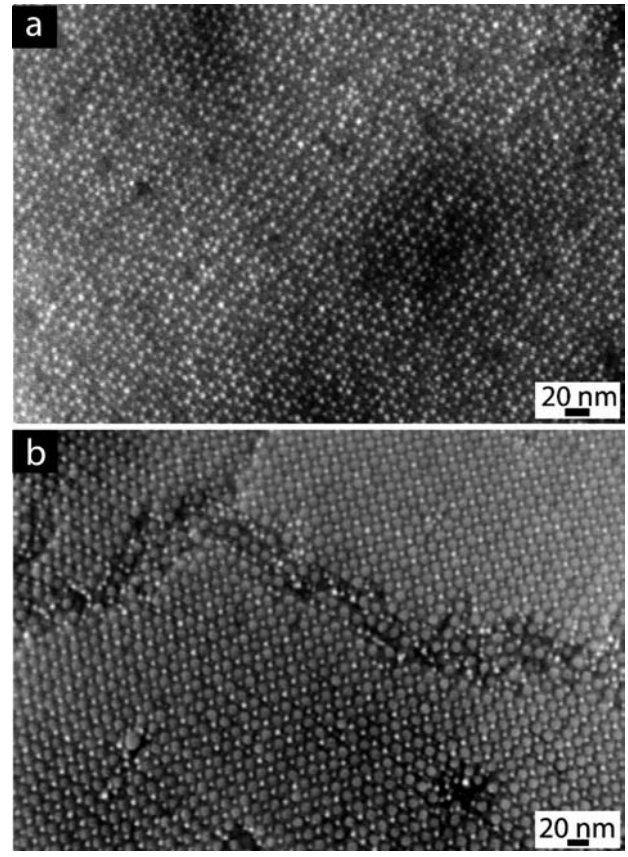

Figure 1. HRSEM images of sh-AB_2 BSLs on Si_3N_4-coated Si substrates with two different exposed BSL crystallographic surfaces: (a) (001) and (b) (100). Crystalline domains up to ~9 μm in diameter were observed. Selected area electron diffraction (SAED) verified the presence of both Au and Fe_2O_3 nanocrystals in the BSLs (Figure S2 in Supporting Information).

with the smaller Au nanocrystals filling the trigonal prismatic interstitial spaces (See Supporting Information for an illustration of the sh-AB_2 unit cell). Figure 2 shows TEM images of the (100), (110), and (001) surfaces of the BSLs. FFTs of the images index to the sh-AB_2 structure. The (100) and (001) spacings measured in TEM images were 12.6 and 14.1 nm, corresponding to lattice dimensions, $a = 14.5$ nm and $c = 14.1$ nm. From SEM images, the (100) and (001) spacings were found to be 12.2 and 14.4 nm, corresponding to lattice dimensions $a = 14.1$ nm and $c = 14.4$ nm.

Grazing Incidence Small Angle X-ray Scattering (GISAXS). GISAXS measurements were performed on the BSLs and distinct diffraction spots were observed, thus confirming relatively long-range order in the superlattices. Figure 3 shows examples of GISAXS measurements of the BSLs, along with an illustration of the experimental system. All of the measured GISAXS patterns indexed to an sh-AB_2 BSL structure (with a slight lattice contraction of 8−12% normal to the substrate as described below). The diffraction spot sizes varied from broad to narrow features, indicating variability in the size of crystalline BSL grains and their crystallographic superlattice orientations with respect to the substrate. Additional SEM images of BSLs are included in the Supporting Information, which clearly show that the BSL samples consist of multiple crystal grains with a variety of orientations on the substrate.

The GISAXS measurement in Figure 3a exhibits broad Bragg spots. These broad spots indicate that the scattering BSL grains are relatively small. The diffraction pattern indexes to a slightly

(45) Gruner, S. M.; Tate, M. W.; Eikenberry, E. F. *Rev. Sci. Instrum.* **2002**, *73*, 2815–2842.
(46) Hammersley, A. P. ESRF Internal Report, 997, *ESRF97HA02T*.
(47) Tate, M. P.; Urade, V. N.; Kowalski, J. D.; Wei, T. C.; Hamilton, B. D.; Eggiman, B. W.; Hillhouse, H. W. *J. Phys. Chem. B* **2006**, *110*, 9882–9892.
(48) Smilgies, D.-M.; Blasini, D. R. *J. Appl. Crystallogr.* **2007**, *40*, 716–718.

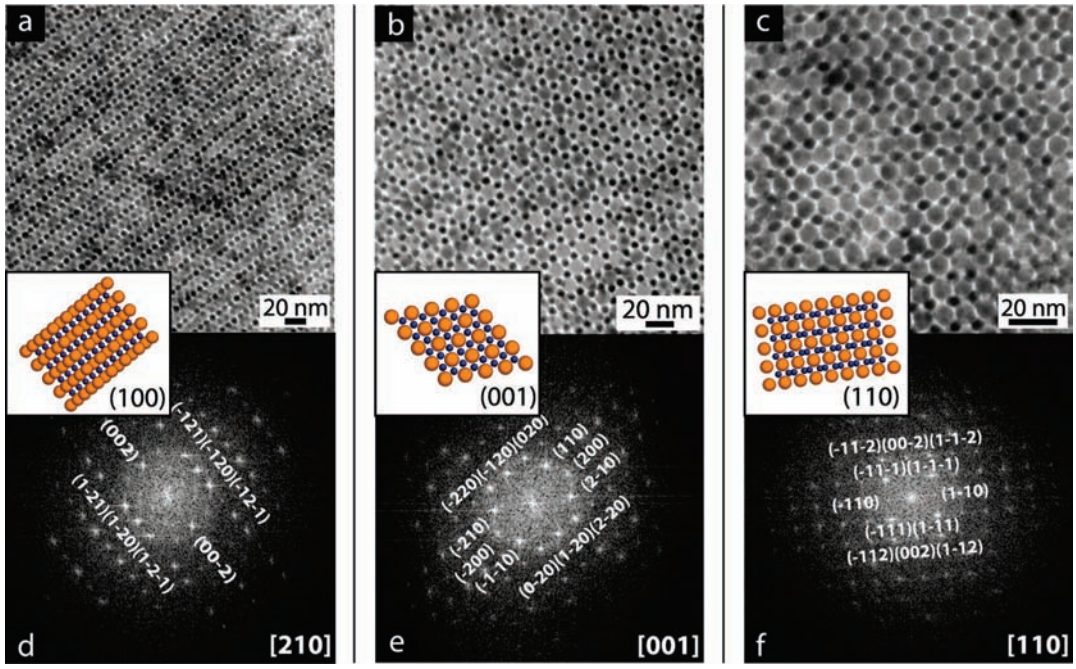

Figure 2. TEM images and FFTs of sh-AB_2 BSLs observed down three different zone axes to provide images of the corresponding lattice planes: (a,d) [210], (100); (b,e) [001], (001); and (c,f) [110], (110). The FFTs are indexed to sh-AB_2 lattice planes; the zone axes are given in the bottom right of the FFTs. Crystallographic models of the sh-AB_2 superlattices are provided in the insets; blue and orange spheres represent Au and Fe_2O_3 nanocrystals, respectively.

distorted sh-AB_2 superlattice (AlB_2 analog, SG 191, *P6/mmm*) oriented on its (100) plane on the substrate with unit cell dimensions of $b = c = 13.8$ nm, $a = 12.7$ nm and $\gamma = 123.0°$. This structure corresponds to a simple hexagonal lattice with a uniaxial lattice contraction of 11% normal to the substrate in the [210] direction. This crystal structure is equivalent to a centered orthorhombic lattice oriented on a (010) plane with unit cell dimensions $a = c = 13.8$ nm, $b = 21.273$ nm (SG 65, *Cmmm*).

The GISAXS data in Figure 3a indicate that the sh-AB_2 BSL initially formed on the substrate with lattice dimensions of 13.8 nm and then contracted unidirectionally toward the substrate. This type of contraction normal to the substrate has been observed in other evaporated films as well, of ordered block copolymers,[49] mesoporous metal oxides,[50] and gold nanocrystal superlattices.[51] The lattice contraction results from the evaporation of residual solvent retained by the capping ligands just after BSL formation (Figure 4). As the residual solvent evaporates, the superlattice shrinks. But the nanocrystals cannot move laterally with respect to the substrate because their positions are fixed by adhesion to the substrate and as a result, the lattice decreases its total volume with a uniaxial compression toward the substrate.

In addition to the diffraction spots in Figure 3a that index to sh-AB_2 BSL oriented on a (100) plane that has contracted in the [210] direction, there are two diffraction spots (labeled in gray) corresponding to sh-AB_2 BSL grains with a different crystallographic orientation on the substrate. These spots index to sh-AB_2 BSL grains oriented on their (001) planes that have contracted in the [001] direction, with unit cell dimensions of $a = b = 13.8$ nm, $c = 12.3$ nm.

The GISAXS patterns could not be indexed without considering the lattice contraction and the appropriate crystallographic orientation of the BSL grains on the substrate. Figure 3b provides another GISAXS example that reveals information about the superlattice orientation on the substrate and the uniaxial lattice compression that occurs perpendicular to the substrate. Both broad and narrow diffraction spots are present in Figure 3b, corresponding to relatively small and large superlattice grains, respectively. The broader diffraction spots indexed to a (100)-oriented sh-AB_2 BSL with lattice dimensions of 13.8 nm and a uniaxial lattice compression of 12% in the [210] direction. One set of the narrower diffraction spots indexed to a (100)-oriented sh-AB_2 superlattice with lattice dimensions of 14.3 nm that has contracted by 8% normal to the substrate in the [210] direction. These data indicate that more lattice shrinkage has occurred in the smaller BSL grains than in the larger grains.

Figure 3c shows another example of a GISAXS pattern obtained from an Au/Fe_2O_3 nanocrystal BSL sample. The "rings" of small spots suggest that a coexistence of many large superlattice grains with varying orientations exists on the substrate. One set of diffraction spots indexes to an orthorhombic BSL oriented in the [010] direction normal to the substrate with unit cell dimensions $a = c = 14.2$ nm, $b = 22.628$ nm (corresponding to a sh-AB_2 lattice with initial unit cell dimensions of 14.2 nm that has been compressed in the [210] direction by 8%). The ring-like diffraction pattern provides averaged information about the structure of the BSL grains since the grains have various crystallographic orientations. Indexing this pattern is complicated by the fact that BSL grains will have slightly different lattice *symmetry* depending on their orientation on the substrate due to the difference in the lattice direction of the uniaxial shrinkage. Nonetheless, the pattern can be ap-

(49) Bosworth, J. K.; Paik, M. Y.; Ruiz, R.; Schwartz, E. L.; Huang, J. Q.; Ko, A. W.; Smilgies, D. M.; Black, C. T.; Ober, C. K *ACS Nano* **2008**, *2*, 1396–1402.
(50) Ruland, W.; Smarsly, B. M. *J. Appl. Crystallogr.* **2007**, *40*, 409–417.
(51) Dunphy, D.; Fan, H.; Li, X.; Wang, J.; Brinker, C. J. *Langmuir* **2008**, *24*, 10575–10578.

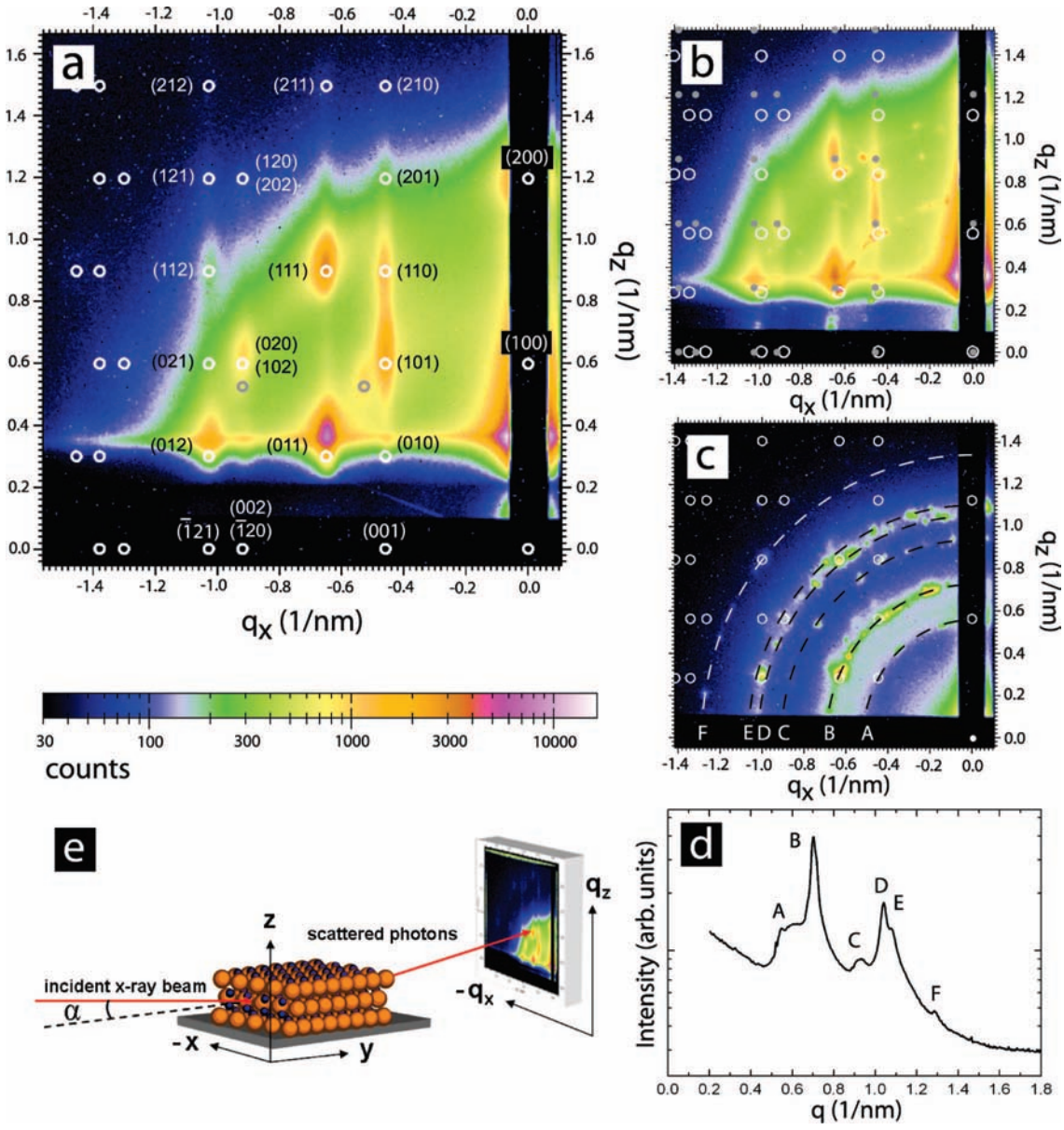

Figure 3. GISAXS measurements of BSLs assembled with 6.1 and 11.5 nm Au and Fe_2O_3 nanocrystals. The white circles in (a) correspond to the simulated diffraction spot pattern for a slightly distorted sh-AB_2 BSL with lattice dimensions $b = c = 13.8$ nm, $a = 12.7$ nm, $\gamma = 123.0°$, which corresponds also to a centered orthorhombic (SG 65, *Cmmm*) unit cell oriented with the [010] direction normal to the substrate with dimensions $a = c = 13.8$ nm, $b = 21.273$ nm. The gray circles in (a) correspond to (011) and (111) spots of an sh-AB_2 lattice oriented with the crystallographic direction [001] normal to the substrate with unit cell dimensions of $a = b = 13.8$ nm, $c = 12.3$ nm. (See Supporting Information for a complete simulation and indexing of the (001) orientation, Figure S6.) (b) Simulated diffraction spots for sh-AB2 BSLs oriented on (100) planes with unit cell dimensions and a uniaxial lattice compression in the [210] direction of (gray dots) 13.8 nm, 12% and (white circles) 14.3 nm, 8% (which corresponds to a centered orthorhombic (SG65, *Cmmm*) lattice oriented in the [010] direction normal to the substrate with unit cell dimensions of (gray dots) $a = c = 13.8$ nm, $b = 21.0$ nm, and (white circles) $a = c = 14.3$ nm, $b = 22.8$ nm.) (c) Scattering pattern with rings of small spots indicated with dashed lines (A−F). (d) Radial integration of the scattering data in (c); Table 1 provides the q-values, d-spacings, and indices of the GISAXS data. (e) Schematic of the GISAXS configuration: incident X-ray beam, sample and sample manipulation, scattered beams, and area detector.

proximately indexed to a simple hexagonal lattice, with the corresponding d-spacings obtained from the q-values of the diffraction rings, $q = 2\pi/d$, provided in Table 1. Indexing the GISAXS data to an sh-AB_2 lattice gave lattice constants between 13.29 and 14.01 nm, which are consistent with what was found by TEM and SEM. But there is also a slight, but noticeable, anisotropy in the scattering rings. The diffraction features occur at slightly higher q in the x-direction than in the z-direction, which provides further indication of the lattice shrinkage normal to the substrate. Therefore, three different values of q (q_x, q_z, and $<q>$) are provided in Table 1 for the scattering peak positions. The difference in these averaged lattice constants shows that the shrinkage is ∼7%.

Dislocations in sh-AB2 BSLs. Bright stripes of nanocrystals were visible in SEM images of some BSLs formed on Si_3N_4 wafers, as shown in Figure 5. Additional SEM images of BSLs with these defects are provided in the Supporting Information. The stripes were observed in superlattices with the (100) plane parallel to the substrate and were identified to be superlattice dislocations consisting of gold nanocrystal half-planes inserted into the lattice as illustrated in Figure 5. Tilting the sample and imaging by SEM confirmed that the stripes were not step edges.

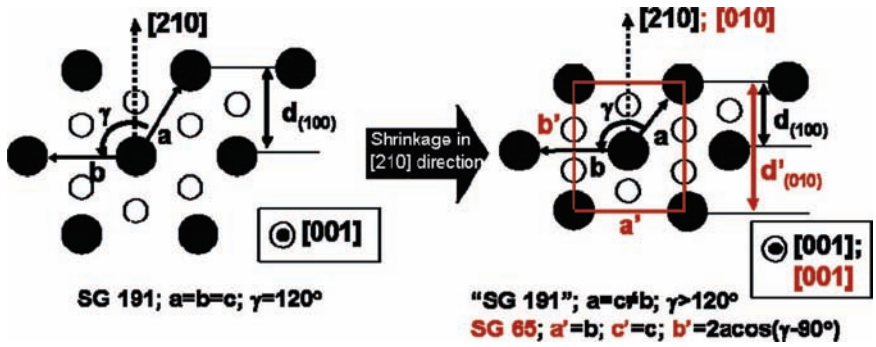

Figure 4. Depiction of the lattice contraction of a sh-AB_2 BSL that has contracted in the [210] direction during the late stages of drying. The BSL is oriented on its (100) plane parallel to the substrate contraction in the [210] direction normal to the substrate changes the lattice symmetry from hexagonal to centered orthorhombic. The centered orthorhombic unit cell dimensions, *a*', *b*', *c*' are shown in red.

Table 1. Measured *d*-Spacings from the GISAXS Patterns in Figures c Compared to the Calculated *d*-Spacings for an sh-AB_2 Lattice (given in parentheses)[a]

ring	q_x (nm^{-1})	$d = 2\pi/q_x$ (nm)*	q_z (nm^{-1})	$d = 2\pi/q_z$ (nm)†	<q>[b] (nm^{-1})	$d = 2\pi/\langle q \rangle$ (nm)‡	indexed planes
A	0.51	12.320 (12.134)	0.55	11.424 (11.510)	0.55	11.424 (11.668)	{100}
B	0.68	9.240 (9.172)	0.72	8.727 (8.701)	0.70	8.976 (8.820)	{101}
C	0.90	6.981 (7.006)	0.935	6.720 (6.646)	0.935	6.756 (6.737)	{110}
D	1.01	6.221 (6.266)	1.05	5.984 (5.944)	1.05	6.041 (6.025)	{111}
E	1.06	5.928 (6.067)	1.10	5.712 (5.755)	1.10	5.818 (5.834)	{200}
F	1.28	4.909 (4.954)	1.34	4.689 (4.699)	1.34	4.689 (4.764)	{112}

[a] *d*-Spacings calculated for a simple hexagonal lattice (SG191) with lattice constants $a = b = c = 14.01$nm,* $a = b = c = 13.29$nm,† and $a = b = c = 13.47$nm.‡;. [b] Average q values obtained from the radial integration of the GISAXS data in Figure 3c.

A correlation between the dislocation direction in neighboring superlattice islands, like those in Figures 5b and Figure 6, was observed. The inset in Figure 6 shows a histogram of the dislocation orientation measured from many BSL islands that were deposited on one substrate. The average dislocation orientation relative to the horizon in the figure is 28.6°. These islands appear to break off from a common BSL layer that forms at the air/solvent interface to deposit on the substrate. Although the drying direction is not known, the dislocation direction most likely occurs at 90° with respect to the drying direction, as illustrated in the figure, arising from the strain imposed on the BSL from the curved air/solvent interface as illustrated in Figure 7. The dislocations relieve this strain as the superlattice forms.

Monolayers and Defects. An expansion of sh-AB_2 superlattice planes was observed in some thin superlattice layers. Figure 8a shows an example of such a sh-AB_2 superlattice, which has an unexpectedly large lattice constant of $c = 15.9$ nm, compared to $c = 14.1$ nm observed in thicker sh-AB_2 superlattice films such as those in Figures 8, parts b and c. The thin nanocrystal layer in the lower right corner of Figure 8a corresponds to a (100) sh-AB_2 plane.

The TEM image in Figure 8a reveals a case in which the BSL structure (with the (100) plane parallel to the substrate) appears to assemble from a monolayer on the substrate into ordered multilayers. Another TEM image in Figure 8c shows an example of sh-AB_2 superlattices with lower nanocrystal layers that are disordered, suggesting that in this case, the superlattices formed in solution and their assembly was not directed by the solution−substrate interface. Therefore, the influence of the substrate on BSL nucleation is presently not entirely clear, but perhaps when the superlattices nucleate on the substrate their lattice dimensions are directed by the substrate, which can give rise to an "expanded" unit cell like that in Figure 8a or a BSL structure different than the sh-AB_2 structure.

A new BSL structure was also observed that is similar to a (100) plane of a cuboctahedron AB_{13} superlattice (space group 226, $Fm\bar{3}c$) with Au nanocrystals substituted for Fe_2O_3 nanocrystals at the 8a Wyckoff positions in the unit cell (of space group 226). Figure 9 shows a TEM image of this structure. This BSL structure was observed only in thin nanocrystal layers. Although this structure is not equivalent to a cuboctahedron AB_{13} superlattice, it is structurally very similar and is not surprising that it coexists with the AB_2 superlattices since the coexistence of AB_2 and AB_{13} superlattices has been observed in a number of cases, including hard sphere colloidal particles[52−55] and binary nanocrystal superlattices.[2,3]

Discussion

BSL Formation and Space-Filling in the sh-AB2 Lattice. All of the BSLs were made by slowly evaporating the solvent from concentrated dispersions with added oleic acid on tilted substrates. Phase segregation of Au and Fe_2O_3 nanocrystal superlattices was regularly observed (see Supporting Information for an example) when oleic acid was not added in excess to the dispersion. Also, when the nanocrystals were deposited on flat substrates, BSLs were not observed. These observations indicate that the forces directing BSL formation are surprisingly subtle.

Various driving forces for BSL formation have been mentioned in the literature,[2,3,7,8] but there is currently no consensus as to which forces are most influential. Some of this uncertainty probably stems from the complicating interactions of the deposition substrate, particularly in the case of thin BSL films, which have exhibited a variety of different structures. Certainly, one of the primary driving forces of BSL formation is the increase in "free volume" entropy that occurs when the

(52) Cottin, X.; Monson, P. A. *J. Chem. Phys.* **1995**, *102*, 3354–3360.
(53) Murray, M. J.; Sanders, J. V. *Philos. Mag. A* **1980**, *42*, 721–740.
(54) Schofield, A. B.; Pusey, P. N.; Radcliffe, P. *Phys. Rev. E* **2005**, *72*, 031407.
(55) Bartlett, P.; Ottewill, R. H.; Pusey, P. N. *Phys. Rev. Lett.* **1992**, *68*, 3801–3804.

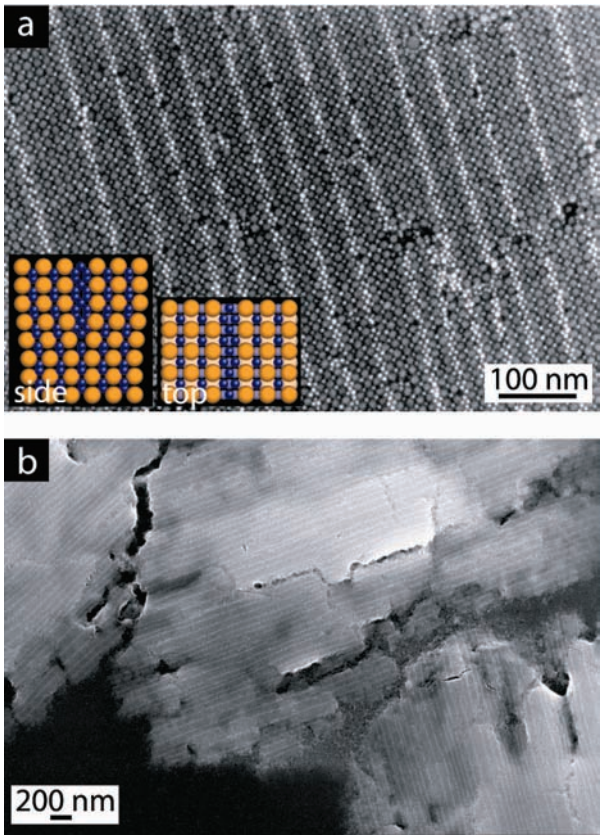

Figure 5. SEM images of superlattice dislocations: nearly periodic bright stripes are observed in these sh-AB_2 BSLs of 11.5 nm Fe_2O_3 and 6.1 nm Au nanocrystals oriented with (100) planes parallel to the substrate. The bright stripes are Au nanocrystal half-planes (dislocations) inserted into the lattice as illustrated in the inset in (a) as viewed from the side (looking at the (1−20) plane down the [010] axis) and from the top (looking at the (100) plane or down the [210] axis as viewed in the SEM images); the blue and orange spheres represent Au and Fe_2O_3 nanocrystals, respectively.

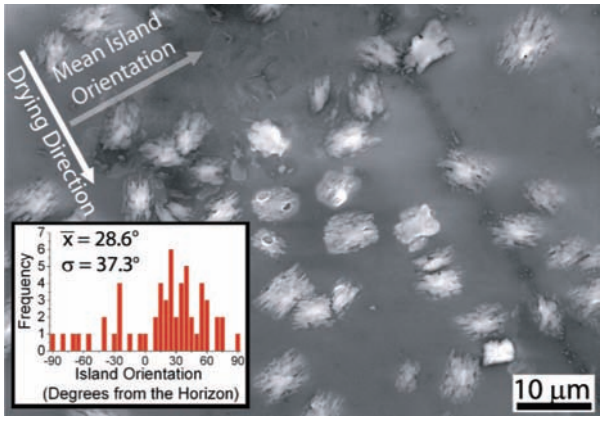

Figure 6. SEM image of BSL islands with visible inserted Au nanocrystal half-planes (dislocations). Inset: the orientational distribution of the dislocation direction with respect to the proposed drying direction indicated in the figure.

bidisperse nanocrystals order into a lattice.[36,37,52,56] The sh-AB_2 lattice is a dense structure and spheres with the right size ratio (the radius ratio of large (R) and small (r) spheres that most efficiently fill space in a sh-AB_2 lattice is $r/R = 0.528$) occupy

(56) Gelbart, W. M.; Ben-Shaul, A. *J. Phys. Chem.* **1996**, *100*, 13169–13189.

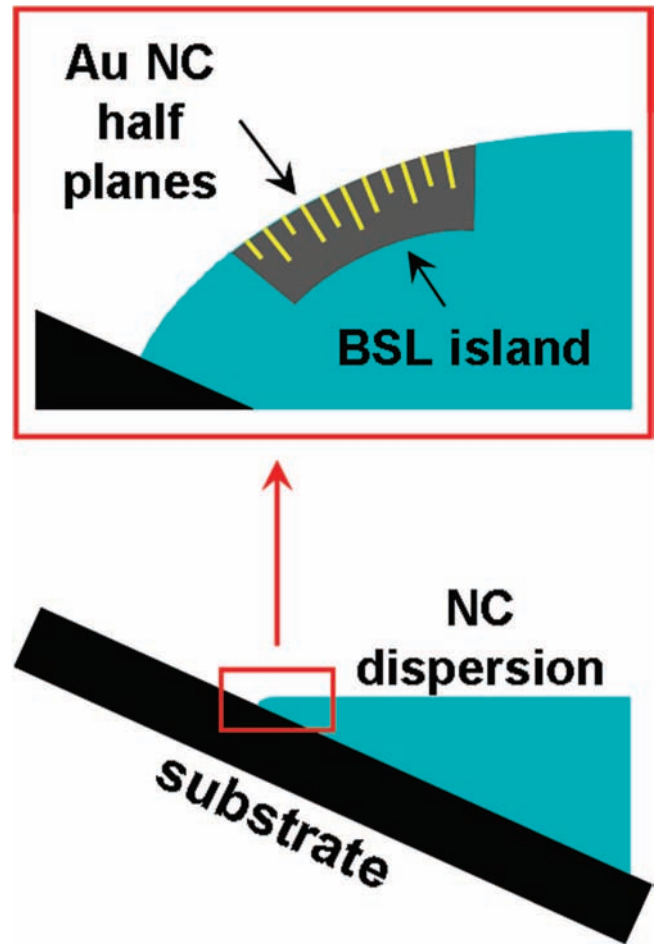

Figure 7. Illustration of the proposed mechanism of dislocation formation in the BSLs: gold nanocrystal half-planes insert into the crystallizing BSL to relieve strain at the curved air/solvent interface near the substrate.

78% of the available volume when ordered into this lattice—this is denser than a face-centered cubic (fcc) lattice (74%) of monodisperse spheres and nearly as dense as the closest-packed rock salt lattice (79%, but only for a radius ratio of 0.414; a rock salt lattice with a radius ratio of 0.528 is much less dense than the sh-AB_2 structure).

The Au and Fe_2O_3 nanocrystals used in this study are nearly perfectly size-matched for forming sh-AB_2 BSLs. From the interparticle spacing measured by GISAXS, the *effective* radii of Au and Fe_2O_3 nanocrystals are 3.8 and 7.15 nm, which corresponds to $r/R = 0.531$. The nanocrystals exhibit an effective radius in the superlattice that consists of the inorganic cores, which are 3.05 and 5.75 nm for the Au and Fe_2O_3 nanocrystals, along with the additional space occupied by the ligands that fill the space between the inorganic surfaces in the superlattice. The volume filled by ligands is determined experimentally from the combination of the GISAXS measurements that reveal the BSL unit cell dimensions and electron microscopy, which provides the inorganic core sizes. The experimentally determined ligand volume in the BSLs compares well to the expected excluded volume for nanocrystals with monolayer capping ligand coverage, to within ± 10%.[57] The Au and Fe_2O_3 nanocrystals pack together into ordered superlattices of "soft spheres," as described previously for the case of superlattices of monodisperse ligand-stabilized nanocrystals.[36,37] For these

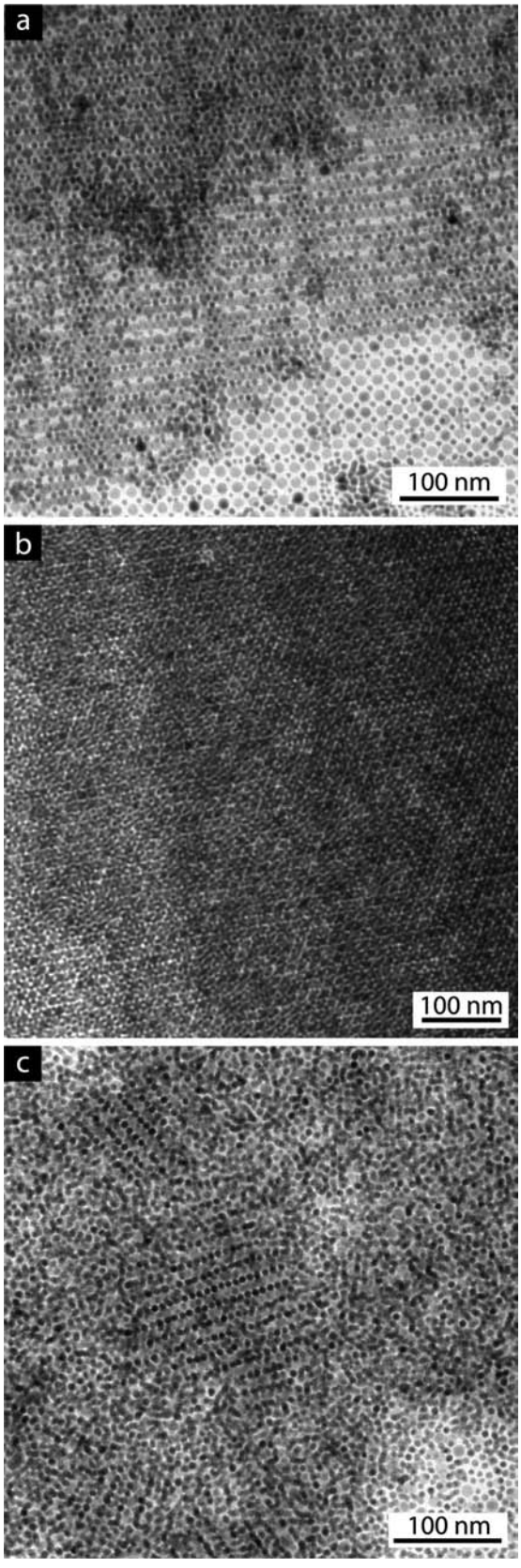

Figure 8. TEM images of thin sh-AB_2 BSLs. In (a) and (b) the superlattices appear to have nucleated on the substrate and crystallized from the bottom of the image to the top in (a) and from the left to the right in (b). The (100) plane is parallel to the substrate in image (a) and the (001) plane is parallel to the substrate in (b). In (c), the nanocrystals on the substrate are disordered and the BSL (with (100) orientation parallel to the substrate) does not appear to have nucleated on the substrate.

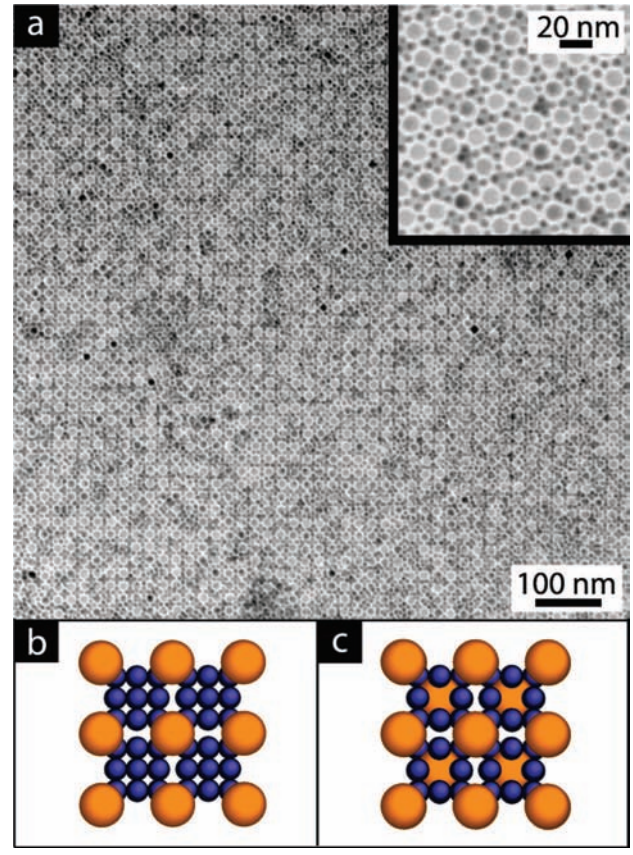

Figure 9. (a) TEM image of a two-dimensional BSL (a monolayer) with structure similar to the (100) plane of a cuboctahedron AB_{13} superlattice. The inset shows a higher magnification image. (b) Three-dimensional model of space group 226, a cuboctahedron AB_{13} superlattice. (c) Three-dimensional representation of a superlattice with Fe_2O_3 nanocrystals (orange) in place of Au nanocrystals (blue) at the 8a Wyckoff positions in the unit cell of space group 226.

nearly ideal sh-AB_2 BSLs, there is no need to believe that exotic forces between nanocrystals, such as electrostatic charging, are playing a role in their formation; although there is no evidence here that would discount their presence either.[58]

Depletion Attraction and its Possible Role in BSL Formation. Additional attractive forces can further enhance BSL formation, as well as disrupt it. Van der Waals attractions,[36,37] ligand−ligand interactions,[38] capillary forces,[39] and electrostatic

(57) From TEM, the inorganic Au and Fe_2O_3 cores are 6.1 and 11.5 nm in diameter. The fully extended ligand length, L, was computed using the fact that dodecanethiol and oleic acid have hydrocarbon chain lengths n, of 12 and 18: $L = 0.154 + 0.127n$ (nm).[62] Since the unit cell contains one Fe_2O_3 and two Au nanocrystals, the volume taken up by the inorganic cores of the Au and Fe_2O_3 nanocrystals in the unit cell is 1034.02 nm^3. The total unit cell volume determined from GISAXS is 2552.32 nm^3. Assuming that the Au and Fe_2O_3 nanocrystals are coated with a monolayer of ligands, the ligands have total excluded volumes of 233 nm^3 and 1209 nm^3, respectively. These values are calculated by using the relation, $v = (27.4 + 26.9n) \times 10^{-3}$ (nm^3) for the excluded volume v, of each ligand molecule,[62] and estimating the number of ligands bound to each nanocrystal by taking a circular molecular "footprint" of 16 $Å^2$/molecule and assuming a close-packed monolayer with 91% surface coverage (the surface coverage of a hexagonal close-packed layer of disks).[36] From the GISAXS measurements of the BSL unit cell dimensions inorganic core sizes measured by TEM, the ligands must occupy (1990.81 nm^3 + 561.51 nm^3)− 1034.02 nm^3 = 1518.30 nm^3, which is very close to the estimated excluded volume of the ligands assuming close-packed capping ligand monolayers on the nanocrystals, which is 1209 nm^3 + (2 × 233 nm^3) = 1675 nm^3—a difference of ∼9%.

interactions[2] have been proposed to be important. One force that has not been discussed to any significant extent with respect to BSL formation is the *depletion attraction* between nanocrystals that can be induced by the excess free oleic acid in the dispersion. Depletion attraction forces can arise between two bodies—such as two nanocrystals—immersed in a solution with macromolecules.[56,59] Depletion attraction forces are typically important when the macromolecule is less than about one tenth the size of the nanocrystal and can easily move out of the intervening space between the particles, which is certainly the case of an oleic acid molecule. When the interparticle separation becomes less than the diameter of the macromolecule, the macromolecule is pushed out of the intervening solvent, which leads to an osmotic force that drives the solvent out from between the particles and pushes them together. Asakura and Oosawa[59] first showed that such an attractive force F develops between two spheres of diameter D when the interparticle separation a is less than the size of an intervening macromolecule d:

$$F = -\frac{\pi}{4} p_0 \{(D+d)^2 - a^2\}, D < a < D + d; \quad (1)$$

$$F = 0, a > D + d \quad (2)$$

In eq 1, p_0 is the osmotic pressure of the macromolecular solution, $p_0 = kTN/V$, which in the case of interest is the oleic acid solution. kT is the thermal energy and N/V is the concentration. These expressions show how an increasing oleic acid concentration can enhance the depletion attraction force between nanocrystals. The depletion attraction between nanocrystals become increasingly significant as the solvent evaporates and concentrates the nanocrystals and the oleic acid. The fact that depletion attraction forces are relatively short-range is also important for superlattice formation. These forces help squeeze the nanocrystals together as the solvent evaporates, but do not lead to irreversible particle aggregation—once the macromolecule becomes excluded from between the nanocrystals, the steric repulsion between nanocrystals due to the adsorbed ligands still prevents flocculation. This is important, as the nanocrystals need the ability to orient into their lowest energy structure (i.e., the superlattice).

The Evaporative Front. The other question about BSL formation regards the role of the evaporative front at the liquid−air and liquid-substrate interfaces. Some data indicate that BSLs assemble by nucleating from the substrate, as in the cases shown in Figure 8, parts a and b. In other images, like Figure 8c, ordered BSL domains are resting on a layer of disordered nanocrystals, indicating that the BSLs formed in solution first before depositing on the substrate. Previous studies of gold nanocrystals have found that superlattice monolayers can assemble at the air−liquid interface of an evaporating dispersion.[60] Most of the BSLs studied here appear to crystallize at the air/solvent interface and then deposit onto the substrate as a floating interfacial layer. The curvature of the air/solvent interface leads to strain in the superlattice, which in some cases can lead to dislocations of inserted half-planes of Au nanocrystals in the BSLs with nearly periodic spacing.

Conclusions

Simple hexagonal (sh) AB_2 BSLs of 11.5 nm Fe_2O_3 and 6.1 nm Au nanocrystals were assembled and studied by TEM, SEM, and GISAXS. BSL formation required the slow evaporation of a dispersing solvent with nanocrystal deposition on a tilted substrate. The addition of excess oleic acid to the dispersion solution was also found to be critically important for BSL formation. Excess oleic acid is believed to be inducing depletion attraction forces between the nanocrystals that help overcome the kinetic barrier to BSL formation. The solvent-air-substrate interface is also important, as the BSLs form at this interface.

The GISAXS data showed Bragg spots indicating relatively long-range order in the BSLs. GISAXS also revealed two predominant crystallographic orientations with (100) and (001) lattice planes on the substrate, but (110) oriented BSLs were also observed by TEM. GISAXS revealed a uniaxial shrinkage of 8 to 12% of the superlattice normal to the substrate that is not observable by TEM and SEM since these methods probe the structure by looking perpendicular to the substrate. The lattice shrinkage is the result of the evaporation of residual solvent that is retained in the superlattice right after deposition. For BSLs that have oriented on their hexagonal (100) planes on the substrate, this shrinkage changes the lattice symmetry to orthorhombic.

In addition to the relatively extended sh-AB_2 BSLs, some defect BSL structures were also observed. Nearly periodic dislocations of inserted superlattice half-planes of Au nanocrystals were observed, appearing as bright stripes of nanocrystals in SEM images. A new thin film BSL structure was also observed that is similar to cuboctahedron AB_{13} structure with Fe_2O_3 nanocrystals in place of Au nanocrystals at the 8a Wyckoff positions in the unit cell of space group 226. A relatively large expansion of the sh-AB_2 lattice was also observed when deposited as a thin, near-monolayer film.

BSLs provide an exciting avenue for nanomaterials design. As synthetic methods and self-assembly approaches continue to develop, it is becoming increasingly likely that new materials might be designed systematically and rationally. Presently, however, further experiments are needed to elucidate in detail how BSLs nucleate, the driving forces for BSL formation and the role of the air−solvent−substrate interface on BSL formation. In situ GISAXS to follow BSL assembly in real time might be one next step. The SEM and GISAXS measurements presented here clearly show that BSLs are amenable to such studies.

Acknowledgment. This research was supported by funding from the Robert A. Welch Foundataion, the Air Force Research Laboratory (FA8650-07-2-5061), the National Science Foundation, and the National Institutes of Health (CA 10383). GISAXS measurements were conducted at the Cornell High Energy Synchrotron Source (CHESS) which is supported by the National Science Foundation and the National Institutes of Health/National Institute of General Medical Sciences under NSF award DMR-0225180.

(58) The term, "nearly ideal," is used here to refer to the fact that the BSLs do not strictly have the simple hexagonal lattice symmetry because of their uniaxial lattice shrinkage perpendicular to the substrate that results during the late drying process when residual solvent entrained in the ligands evaporates after the BSL has formed and deposited on the substrate. This slight lattice distortion to an orthorhombic lattice itself is not predicted from simple sphere packing arguments, but easily understood in terms of how the substrate pins the nanocrystals and prevents their restructuring during this late stage of the drying process.

(59) Asakura, S.; Oosawa, F. *J. Chem. Phys.* **1954**, *22*, 1255–1256.
(60) Bigioni, T. P.; Lin, X. M.; Nguyen, T. T.; Corwin, E. I.; Witten, T. A.; Jaeger, H. M. *Nat. Mater.* **2006**, *5*, 265–270.
(61) Whetten, R. L.; Shafigullin, M. N.; Khoury, J. T.; Schaaff, T. G.; Vezmar, I.; Alvarez, M. M.; Wilkinson, A. *Acc. Chem. Res.* **1999**, *32*, 397–406.
(62) Israelachvili, J. *Intermolecular & Surface Forces*, 2nd ed.; Academic Press: San Diego, CA, 1992.

B.G. acknowledges financial support under the NSF IGERT program (DGE-054917). We thank Vince Holmberg, Reken Patel, and Andrew Heitsch for their assistance with substrate preparation, SEM imaging, fruitful discussions, and collecting GISAXS measurements. We also thank Domingo Ferrer for assistance with JEMS software and Elena Shevchenko for insight on the binary superlattice assembly procedure.

Supporting Information Available: Full description and illustration of the preparation parameters and assembly method; SAED pattern from a sh-AB_2 BSL; Illustration of the sh-AB_2 unit cell; TEM images of phase segregated Au and Fe_2O_3 nanocrystal superlattices; Illustration showing how the [210] lattice contraction changes the lattice symmetry to orthorhombic; GISAXS simulation of the diffraction spot pattern produced from an sh-AB_2 (SG191; *P6/mmm*) lattice oriented with the (001) plane parallel to the substrate ([001] direction normal to the substrate) is overlaid onto GISAXS data of binary superlattices of 11.5 nm Fe_2O_3 and 6.1 nm Au nanocrystals; Additional SEM images of the BSLs and inserted Au nanocrystal half-planes (dislocations). This material is available free of charge via the Internet at http://pubs.acs.org.

JA8085438